Dynamical properties of epitaxial ferroelectric superlattices

Y. Kim*
School of Physics, Georgia Institute of Technology, Atlanta, Georgia 30332

R. A. Gerhardt
Materials Science and Engineering, Georgia Institute of Technology, Atlanta, Georgia 30332

A. Erbil†
School of Physics, Georgia Institute of Technology, Atlanta, Georgia 30332
(Received 25 July 1996)

The dynamical properties of epitaxial ferroelectric heterostructures have been investigated by studying the dielectric behavior under external electric field. A phenomenon with a giant permittivity was observed. At low frequencies, real permittivities as high as 420 000 have been measured. Real and imaginary parts of the dielectric constant show large dispersion at high frequencies. In dc measurements, a nonlinear resistance is observed with a well-defined threshold field, correlating with the dc bias-field dependence of ac permittivities. We model these observations as a result of the motion of pinned domain-wall lattices, having sliding-mode motion at high electric fields. The good agreement between the experimental and theoretical results suggests that the deposited interdigitated electrode pattern plays a crucial role in controlling domain-wall dynamics. The pinning of the domain wall comes from a nucleation barrier to the creation of new domain walls. [S0163-1829(97)02310-2]

I. INTRODUCTION

One of the most exciting recent developments in materials science is the ability to produce artificial superlattice structures, which are composed of alternating epitaxial thin films. Many exotic properties have been observed in the artificial superlattice structures made from semiconducting,[1] metallic,[2] magnetic,[3] and superconducting[4] materials.

Ferroelectric superlattices have not been as extensively investigated, despite their possible device applications, including pyroelectric detection, memory systems, and electrooptic modulators. There is also fundamental interest in the study of these artificial structures, since they can have drastically different properties from those of bulk materials.[5] Progress in this area has been relatively slow, because of difficulties in the growth of epitaxial ferroelectric superlattices.

The materials investigated in this paper are perovskite-type $Pb_{1-x}La_xTiO_3$ (PLT) and $PbTiO_3$ (PT) thin films. Bulk PT is cubic at high temperature, and below about 763 K it transforms into a ferroelectric phase with a large tetragonal distortion.[6] Bulk PLT is cubic at room temperature for x values for lanthanum larger than 28%.[7]

Under epitaxial strain, a single-crystal ferroelectric thin film has an equilibrium structure with a periodic array of domain walls.[8,9] Theoretical[10–13] and experimental[8,9,14] studies show that, in ferroelectric thin films, the formation of a periodic domain pattern limits the extension of the interfacial strain field—thus minimizing the total energy of the heterostructure. This is in contrast to an unclamped single-crystal system, in which a single domain is the equilibrium state. It is found that the nature of the domain pattern depends very strongly on the epitaxial mismatch, the film thickness and the measurement temperature.

In a ferroelectric system without defects, a domain wall can move under an external driving force in the host material freely. In a domain-wall lattice, this property is expected to lead to low-energy excitation modes, called dyadons, corresponding to the acoustic waves in the domain-wall lattice.[12] In a perfect system, rigid translation of the domain-wall lattice can take place without an energy barrier. However, nucleation processes and the presence of defects, including dislocations, surface steps, compositional variation, etc., can lead to the pinning of the domain walls. Application of an electric field through an interdigitated electrode deposited on the ferroelectric film produces a periodic strain and a periodic driving force in the film for domain walls. For an external field below a certain threshold, the domain walls can oscillate in the pinned state and their motions are bound. Above the threshold field, the domain-wall lattice can slide continuously to contribute to the dc conductivity, by creating domain walls at one end and annihilating them at the other. The phenomenon is reminiscent of the Frohlich sliding-mode conductivity in charge-density waves[15] and phase-slip resistivity in Josephson junctions in superconductors.[16] In a recent paper,[17] we have reported an observation of a giant permittivity in heterostructures having alternating layers of ferroelectric and nonferroelectric epitaxial oxides.

In the present paper, we expand upon our initial report[17] and provide more complete information on both the theoretical model and the experimental results for the dynamical properties of epitaxial ferroelectric heterostructures. This work encompasses both a description of the dielectric behavior under applied ac- and dc-electric field and a detailed comparison between the theoretical model and the experimental results. In particular, giant permittivity has been investigated in epitaxial PT/PLT heterostructures. A theoretical analysis of experimentally observed giant permittivity was performed

TABLE I. Growth conditions for epitaxial PT/PLT thin-film heterostructures.

Thin film	Flow rate (sccm)	Source temperature (°C)
PLT	O_2:50 Argon through; La: 250 Pb: 140 Ti: 1000	La: 175.5 Pb: 11.5 Ti: 22.0
PT	O_2:8 Argon through; Pb: 100 Ti:1000	Pb: 10.5 Ti: 22.0

by using a model based on the motion of a domain-wall lattice in a sinusoidal washboard potential.

In Sec. II, the experimental aspects of the work, including the thin-film deposition and dielectric constant measurements using interdigitated electrodes, are presented. Section III describes the measured dielectric behavior as a function of ac frequency and dc bias voltage, and the *I-V* characteristics. Section IV provides a detailed treatment of the theoretical model to explain the observed dynamical properties of epitaxial ferroelectric PT/PLT heterostructures. In Sec. V, the experimental results and the theoretical predictions are compared to demonstrate the validity of the model. Finally, Sec. VI provides concluding remarks with recommendations for possible future studies.

II. EXPERIMENTAL METHODS

A. Growth and structural characterization of PT/PLT heterostructures

The epitaxial PT/PLT ferroelectric heterostructures investigated here were grown on (100)-oriented $SrTiO_3$ single-crystal substrates using the metalorganic chemical-vapor deposition technique. The deposition was carried out in an inverted vertical warm-wall reactor with a resistively heated susceptor. The substrate temperature was measured with a *K*-type thermocouple embedded in the susceptor about 1 mm from the substrate. The metalorganic precursors used were tetraethyllead, $Pb(C_2H_5)_4$, lanthanum β-diketonate, $La(C_{11}H_{19}O_2)_3$, and titanium isopropoxide, $Ti(OC_3H_7)_4$, for the PLT thin film while tetraethyllead, $Pb(C_2H_5)_4$, and titanium isopropoxide, $Ti(OC_3H_7)_4$, were used for PT thin films. During the deposition process, the substrate temperature was fixed at 650 °C and the reactor pressure was maintained at 5 Torr. Growth conditions for epitaxial PT/PLT heterostructures are given in Table I. The deposition rates were above 1250 and 1200 Å/h for the PLT and PT thin films, respectively. Particularly, we have studied three superlattices of PT/PLT with modulation wavelengths of 100 Å (sample *S*-40), 400 Å (sample *S*-10), and 2000 Å (sample *S*-2). In each superlattice, PT and PLT layers had equal thickness, and the total thickness was 4000 Å. The first and last layers deposited were PT and PLT, respectively.

The crystal structure was examined by x-ray-diffraction methods using a Siemens digitized horizonal diffractometer employing Cu $K\alpha$ radiation and a sample stage that was equipped with both rotational and rocking capabilities in order to provide statistically correct averaging over the reciprocal-lattice points.

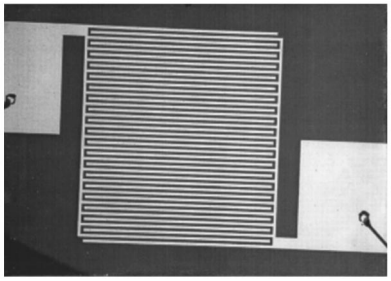

FIG. 1. Interdigitated electrodes on a PT/PLT superlattice, imaged by optical microscopy.

B. Dielectric constant measurements

Since the $SrTiO_3$ substrate is an insulator, the dielectric constant of the epitaxial film cannot be determined by a simple parallel plate capacitor geometry. As an alternative method for capacitance measurement, interdigitated electrodes were deposited by using the photolithographic liftoff technique.

The capacitance for interdigitated electrodes deposited on a film of thickness h (μm) grown on a substrate can be approximated by[18]

$$C=\frac{C_s}{\varepsilon_s+1}\left\{(\varepsilon_s+1)+(\varepsilon_f-\varepsilon_s)\left[1-\exp\left(-\frac{9.2h}{\lambda}\right)\right]\right\}, \tag{1}$$

with

$$C_s=KL(\varepsilon_s+1),$$

$$K=6.5\left(\frac{2d}{\lambda}\right)^2+1.08\left(\frac{2d}{\lambda}\right)+2.37, \quad \text{and} \quad L=(2n-1)l,$$

where λ is the period, n is the number of such periods on the sample, and ε_s and ε_f are the dielectric constant of substrate and film, respectively. Here, K is an empirical value measured in pF/m, with a value of 4.535 for a 1:1 ratio of spacing to width of the interdigitated electrodes. l and d are the length and width of the fingers of electrodes, respectively. This approximation was obtained using the solution of Laplace's equation for the potential in the neighborhood of an interdigitated electrode structure.[19]

The interdigitated electrodes deposited on the sample consist of 20 fingers each with 25 μm spacing and width, and 2 mm long fingers as shown in Fig. 1. All electrodes were deposited under identical conditions. The sample was then integrated onto a pin grid-array package and connections from the film to the package were accomplished by gold wire bonding. Spring loaded gold pins were used to make connections to the leads of the package and these pins were connected to the instrument by low-loss RS58 cables. The capacitance and loss tangent for the $SrTiO_3$ substrate and

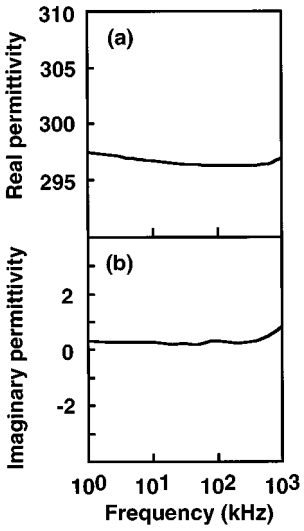

FIG. 2. Frequency dependence of (a) the real and (b) imaginary part of the dielectric constant for a $SrTiO_3$ substrate.

PT/PLT heterostructures were measured by using an HP 4192A impedance analyzer. The real and imaginary part of the dielectric constant were calculated from the measured capacitance and loss tangent of the film by using Eq. (1).

In order to check the validity of this equation for our analysis, an interdigitated electrode was deposited on a $SrTiO_3$ (100) substrate and its dielectric constant determined. As shown in Fig. 2, the measured dielectric constant dependence on frequency was in excellent agreement with the published data of 305–306.[20]

III. EXPERIMENTAL RESULTS

In the following subsections, the structural properties of epitaxial PT/PLT heterostructures are described first. Then, experimental results for the *I-V* characteristics and the ac frequency and dc bias voltage dependence of the complex dielectric constant are presented.

A. Structural properties

In our previous reports,[21,22] x-ray diffraction (XRD), pole figure, and ion channeling experiments have been performed to determine the epitaxial quality of PT/PLT heterostructures. Here, the structural properties of the samples relevant to the dynamical properties are qualitatively described. Figure 3 shows the θ–2θ x-ray-diffraction patterns of the samples *S*-2, *S*-10, and *S*-40. Except for the sample *S*-40 with the smallest modulation wavelength, the samples show ferroelectric transition with the coexistence of *a* and *c* domains in the ferroelectric phase. With decreasing modulation wavelength, the spontaneous strains become smaller, consistent with the earlier observations.[8,9] The sample *S*-40 exhibits a single peak, providing evidence that the superlattice is paraelectric for a modulation wavelength of 100 Å. The broad widths for the peaks of *S*-10 and *S*-2 suggest that different ferroelectric layers in the superlattices have different spontaneous strain values depending on their locations. This would lead to a distribution of parameters for the equilibrium and dynamical properties.

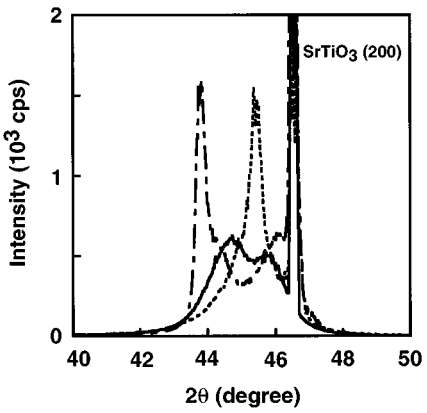

FIG. 3. The θ–2θ x-ray-diffraction patterns for the samples *S*-2 (dot-dashed line), *S*-10 (solid line), and *S*-40 (dotted line).

B. Dispersion in dielectric constant

Figure 4 shows the ac frequency dependence of the real and imaginary parts of the dielectric constant for PT/PLT heterostructures with different modulation wavelengths at zero dc-bais field. Debye-like dispersion of dielectric constants with frequency was observed only for the specimens with modulation wavelengths of 400 and 2000 Å, as shown in Figs. 4(a) and 4(b), respectively. At low frequencies, the real part (ε') of the dielectric constants for *S*-10 and *S*-2 have giant values approaching 420 000 and 350 000, respectively. At high frequencies, ε' approaches the paraelectric-phase dielectric constant of about 750. As would be expected for a sample in the paraelectric phase, ε' for *S*-40 is about 750, and has no significant frequency dependence in the frequency range of 300 Hz–1 Mhz as shown in Fig. 4(c). The imaginary part (ε'') of the dielectric constants for both

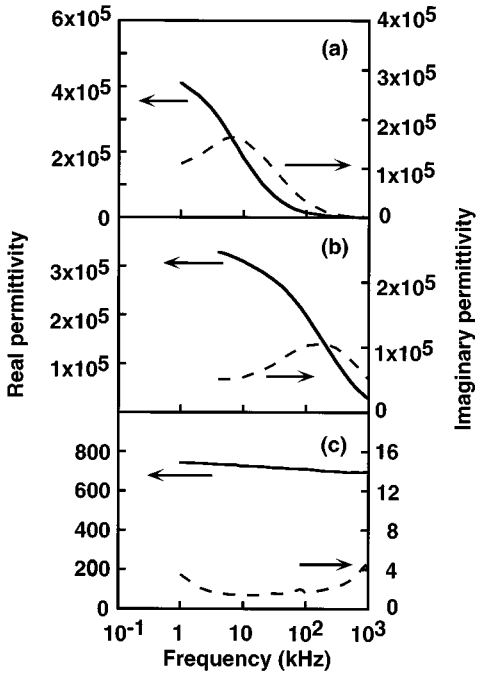

FIG. 4. Frequency dependence of the real (solid line) and imaginary (dashed line) dielectric constants in PT/PLT superlattices of (a) *S*-10, (b) *S*-2, and (c) *S*-40.

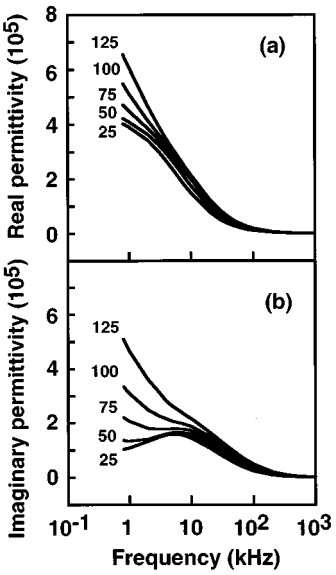

FIG. 5. (a) Real permittivity and (b) imaginary permittivity for the PT/PLT superlattice S-10 as a function of frequency at various temperatures (in °C).

S-10 and S-40 have broad peaks in the frequency range corresponding to the largest dispersions for ε'. A significant temperature dependence of the frequency spectrum for ε' and ε'' of S-10 was measured as shown in Fig. 5. As temperature increases, the dielectric response gets stronger and shifts to lower frequencies.

There could be several possible causes for this type of dielectric dispersion. First, it may be attributable to the metallic layer of the interdigitated electrodes. Since all the electrodes were prepared at the same time under identical conditions, this possibility can be excluded; moreover, the relaxation was observed only from the specimens corresponding to 2000 and 400 Å wavelength modulations. Second, it could be due to the presence of oxygen vacancies in the film. This can be ruled out as well, since all films were prepared under identical growth conditions at a reactor pressure of 5 Torr, and a large amount of oxygen was introduced during the growth. A third possible source is the interfacial polarization space charge. This might be possible as heterostructures have many interfaces to account for. However, the drastic dependence on temperature and frequency cannot be explained through this mechanism. As a final possibility, the motion of the domain lattice of the ferroelectric layers in the heterostructures is suggested. The domain walls in high-quality ferroelectrics can move under the influence of an applied field. This can lead to a very large dielectric response under an alternating electric field at low frequencies.

C. *I-V* characteristics

Measurements of the *I-V* characteristics of the PT/PLT heterostructures were performed by using the interdigitated electrode as two-point probes as shown in Fig. 6. Identical conditions, including temperature and humidity, were maintained for all three samples. To prevent possible permanent damage due to breakdown, voltages were kept below ± 20 V.

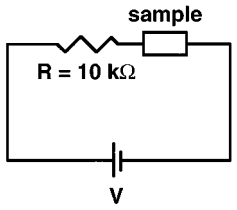

FIG. 6. The circuit used for dc *I-V* characteristic measurements for PT/PLT superlattices.

S-40 was a good insulator within the applied voltage range investigated. Figures 7(a) and 7(b) show dc *I-V* curves taken at room temperature for the S-10 and S-2 samples, respectively. The resistance of each sample was highly nonlinear, and showed well defined threshold voltages V_T of about 5 and 10 V. Both samples were capacitive below V_T and resistive above V_T.

This phenomenon is reminiscent of Frohlich sliding-mode conductivity in charge-density waves[15] and phase-slip resistivity in Josephson junctions in superconductors.[16] Even though the interdigitated electrodes for all the samples were deposited under identical conditions, only S-10 and S-40 exhibit the nonlinear *I-V* characteristics. Therefore, we suggest that the most probable cause for the nonlinear response is the motion of pinned domain-wall lattices, which exhibit sliding-mode motion at high electric fields. We note that S-2 is more conductive than S-10 above V_T. This result is consistent with the observed higher relaxation cutoff frequency for S-2 as shown in Fig. 4.

D. Applied dc–bias voltage dependence of dielectric constants

In order to study the dynamics of the ferroelectric heterostructures (S-2 and S-10) in detail, the applied dc bias voltage dependence of the dielectric behavior at various ac frequencies was measured. The excitation ac signal amplitude was kept at 0.01 V for all frequencies used. The values of both ε' and ε'' are suppressed very strongly at high dc bias fields as shown in Figs. 8(a) and 8(b) for S-10 and Figs. 9(a) and 9(b) for S-2 samples, respectively. The most rapid varia-

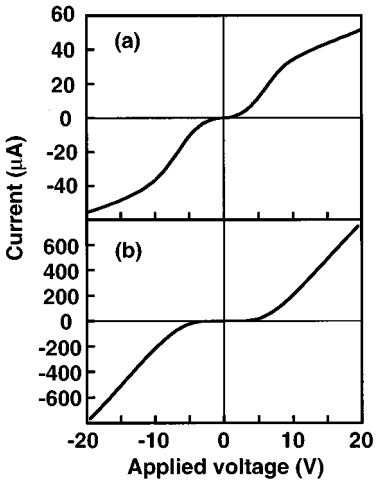

FIG. 7. The dc *I-V* curves at room temperature for the sample (a) S-10 and (b) S-2.

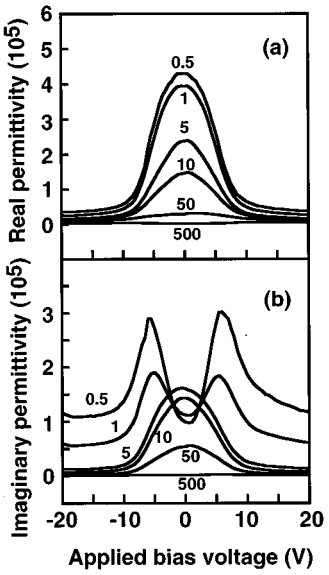

FIG. 8. The measured (a) real and (b) imaginary permittivity as a function of applied dc bias voltage at six different ac signal frequencies for the sample S-10. The numbers labeling the plot are the ac signal frequencies used in kHz.

tions in the dielectric constants for both S-2 and S-10 takes place at or close to the respective threshold voltages observed in the I-V curves. Even though both ε' and ε'' monotonically decrease for most of the frequencies used, we note a complicated variation in ε'' as a function of dc bias voltage at low frequencies for both samples.

IV. THEORETICAL ANALYSIS

A. Rigid-body motion for a domain-wall lattice

As a theoretical interpretation for the observed dielectric behavior, a model based on rigid-body motion of pinned domain-wall lattices is proposed, using the sinusoidal washboard analog. The dielectric behavior of a superlattice subject to an electric field is obtained by assuming an electronic circuit analog as shown in Fig. 10. In this circuit diagram, R represents the resistance for the screening current flow between the electrodes and the domain walls, C_1 is the capacitance associated with the polarization due to domain-wall motion, and C_2 is the capacitance associated with the superlattice in the absence of domain walls.

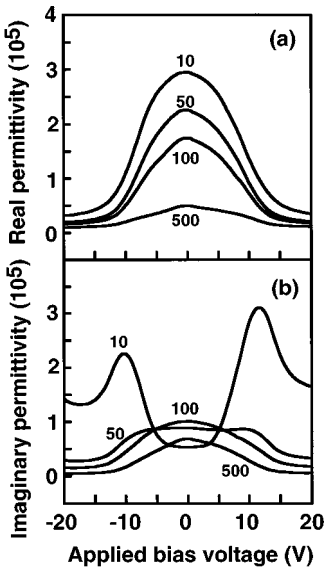

FIG. 9. The measured (a) real and (b) imaginary permittivity as a function of applied dc bias voltage at six different ac signal frequencies for the sample S-2. The numbers labeling the plot are the ac signal frequency used in kHz.

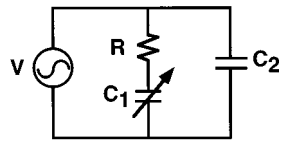

FIG. 10. An electronic circuit analog of the superlattice system.

Figure 11 schematically shows a single domain wall and the relevant parameters in a superlattice. For clarity, the domain walls are shown to be perpendicular to the interface even though in a 90° domain wall the angle is about 45°. This assumption does not change the form of the equations below.

C_1 can be determined by using the equation of rigid-body motion for a domain-wall lattice in a sinusoidal potential, as given by[15]

$$m\ddot{x}+\gamma\dot{x}+\frac{2\pi e_d Lh}{\lambda}\sin\frac{2\pi}{\lambda}x-LhP_sE=0. \tag{2}$$

In Eq. (2), m and γ are the mass and the intrinsic damping parameters, respectively. x is the domain-wall position. e_d is the domain-wall pinning energy per unit area, and L and h are the lateral dimensions of a domain wall as shown in Fig. 11. λ is the period of the pinning potential, and P_s is the value of permanent polarization. E is the effective average field driving the motion, determined by taking into account the complex field distribution on the superlattice due to the electrodes.[19] It is expected that E is proportional to the applied voltage V between the interdigitated electrodes, with a proportionality constant a:

$$E=E_{\mathrm{dc}}+E_{\mathrm{ac}}=a(V_{\mathrm{dc}}+V_{\mathrm{ac}}). \tag{3}$$

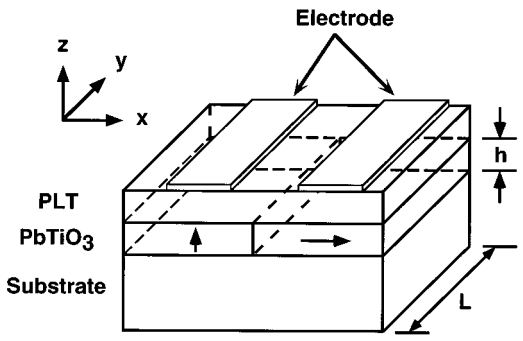

FIG. 11. Schematic diagram of a ferroelectric-nonferroelectric heterostructure with one period. The arrows represent the polarization directions within the domains.

In Eq. (2), the first and second terms can be ignored, since they will be important only at frequencies close to the microwave frequencies. Therefore, Eq. (2) can be modified as

$$\sin\frac{2\pi}{\lambda}x=\frac{P_s\lambda}{2\pi e_d}E. \tag{4}$$

The current due to domain-wall motion is given by

$$I=\frac{dq}{dt}=P_sL\frac{dx}{dt}=P_sL\frac{dx}{dE}\frac{dE}{dt}=j\omega P_sL\frac{dx}{dE}E_{\rm ac}, \tag{5}$$

where q is the polarization charge.

From Eq. (4),

$$\frac{dx}{dE}=\frac{P_s\lambda^2}{4\pi^2e_d}\frac{1}{\cos[(2\pi/\lambda)x]}=\frac{P_s\lambda^2}{4\pi^2e_d}\frac{1}{\sqrt{1-\sin^2[(2\pi/\lambda)x]}}, \tag{6}$$

or

$$\frac{dx}{dE}=\frac{P_s\lambda^2}{4\pi^2e_d}\frac{1}{\sqrt{1-[(P_s\lambda/2\pi e_d)E]^2}}. \tag{7}$$

Therefore, Eq. (5) becomes

$$I=j\omega P_sL\frac{P_s\lambda^2}{4\pi^2e_d}\frac{1}{\sqrt{1-[(P_s\lambda/2\pi e_d)E]^2}}E_{\rm ac}. \tag{8}$$

The capacitance C_1 can be obtained as

$$C_1=P_sL\frac{P_s\lambda^2a}{2\pi^2e_d}\frac{1}{\sqrt{1-[(P_s\lambda/2\pi e_d)E]^2}}. \tag{9}$$

In the presence of both an ac signal ($V_{\rm ac}$) and a dc bias ($V_{\rm dc}$), if $V_{\rm ac}\ll V_{\rm dc}$ the capacitance C_1 can be expressed as

$$C_1=C_{10}\frac{1}{\sqrt{1-(V_{\rm dc}/V_T)^2}}, \tag{10}$$

where

$$V_T=\frac{2\pi e_d}{\lambda P_s a}, \tag{11}$$

and

$$C_{10}=\frac{L\lambda P_s}{2\pi V_T}. \tag{12}$$

Here, C_{10} is the capacitance due to domain-wall motion at $V_{\rm dc}=0$ V, while V_T is the threshold voltage.

B. Field distribution around interdigitated electrodes

The field distribution is of importance because it determines the effective driving force. In our configuration, only the vertical components of the electric field would play an important role in the domain-wall dynamics.

As shown in Fig. 11, the xy plane represents the plane of the film. Given the assumption that the thickness of the metal strips is negligible compared to the period in the x direction, the vertical component of the electric field E_z inside the film is given by[23]

$$E_z=mG(\Delta)\left(\frac{2\pi}{p}\right)\left\{\sum_{n=0}^{\infty}P_n(\cos\Delta)\exp\left[-j\left(n+\frac{1}{2}\right)\left(\frac{2\pi}{p}\right)(x+jmz)\right]+\sum_{n=0}^{\infty}P_n(\cos\Delta)\exp\left[j\left(n+\frac{1}{2}\right)\left(\frac{2\pi}{p}\right)(x-jmz)\right]\right\}, \tag{13}$$

where

$$m=\sqrt{\frac{\varepsilon_{11}}{\varepsilon_{33}}}\quad\text{and}\quad\Delta=\frac{\pi d}{p},$$

$P_n(x)$ is the Legendre polynomial of order n, p is the sum of the spacing and the width of the electrode (i.e., half period), while d is the finger width. ε_{11} and ε_{33} are two of the dielectric tensor elements of the film. Here, $G(\Delta)$ is a normalization constant given by the expression

$$G(\Delta)=-\frac{1}{4K'(s)}, \tag{14}$$

where $s=\sin(\Delta/2)$, and $K'(s)$ is the complete elliptic integral of the first kind of the complementary modules $s'=\sqrt{1-s^2}$.

Since $d=25\ \mu$m, $p=50\ \mu$m in our experiments,

$$\Delta=\frac{\pi}{2},\quad s=\sin\frac{\pi}{4}=\frac{1}{\sqrt{2}},\quad s'=\sqrt{1-\frac{1}{2}}=\frac{1}{\sqrt{2}}.$$

Therefore,

$$K'(s)=K(s)=2.086\quad\text{and}\quad G(\Delta)=G\left(\frac{\pi}{2}\right)=-0.1198.$$

Thus, the equation for E_z takes the following form for our geometry:

$$E_z=-0.2397\left(\frac{2\pi}{p}\right)\sum_{n=0}^{\infty}P_n(0)\exp\left[\left(n+\frac{1}{2}\right)\frac{2\pi z}{p}\right]\times\cos\left[\left(n+\frac{1}{2}\right)\frac{2\pi x}{p}\right]. \tag{15}$$

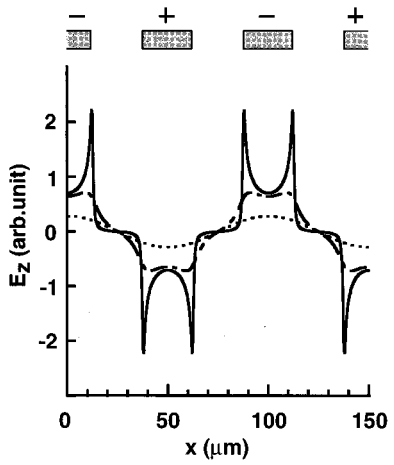

FIG. 12. Plot of the x dependence of the electric field calculated at 100 Å (solid line), 2000 Å (dot-dashed line) and 4000 Å (dotted line) below the interdigitated electrodes. The location and polarity of the electrodes are shown at the top.

Figure 12 shows plots of x dependence of the electric-field distribution calculated at 100 Å (solid line), 2000 Å (dot-dashed line), and 4000 Å (dotted line) below the interdigitated electrodes. The field is very sharp at the edges of the fingers with very large variation between adjacent electrodes at close distances. These sharp opposing electric fields play a crucial role in controlling domain-wall dynamics.

C. Determination of complex permittivity

A capacitor with a geometrical capacitance C_0 has admittance:[24]

$$Y=\frac{1}{Z}=(\varepsilon''+j\varepsilon')\omega C_0. \tag{16}$$

Here, ω is the angular frequency for the applied ac signal and C_0 is the capacitance of the interdigitated electrode pattern in vacuum. C_0 is equal to 0.36 pF for the electrode pattern used.

The admittance of the electronic circuit shown in Fig. 10 is

$$Y=j\omega C_2+\frac{1}{Z_1}=j\omega C_2+\frac{j\omega C_1}{1+j\omega RC_1} \tag{17}$$

where Z_1 is the impedance of the partial circuit RC_1.

If the capacitor C_1 is charged to a voltage V_0 and then the circuit is shorted across the RC_1 combination, the voltage V_1 across the condenser will decrease as a function of time and cause a current flow $C_1(dV_1/dt)$ through the resistor. The voltage drops exponentially according to a relaxation time for the polarization charge associated with domain-wall motion:

$$\tau=RC_1. \tag{18}$$

Introducing τ into Eq. (17) and separating the real part from the imaginary, the admittance can be expressed as

$$Y=\frac{\omega^2C_1\tau}{1+\omega^2\tau^2}+j\omega C_2+\frac{j\omega C_1}{1+\omega^2\tau^2}. \tag{19}$$

The admittance for the case of $V>V_T$ can be expressed as

$$Y=\frac{-C_1\omega^2\tau}{1-\omega^2\tau^2}+j\omega C_2+\frac{\omega C_1}{1-\omega^2\tau^2}=\frac{\omega C_1}{1+\omega\tau}+j\omega C_2, \tag{20}$$

while for the case of $V<V_T$, the admittance is simply the same as given in Eq. (19). By dividing Eqs. (19) and (20) by ωC_0, the real and imaginary permittivity can be determined, as

$$\varepsilon'=\begin{cases}\dfrac{\varepsilon_1+\varepsilon_2+\varepsilon_2\tau^2\omega^2}{1+\tau^2\omega^2} & \text{for} \quad |V|<V_T \\ \varepsilon_2 \quad \text{for} \quad |V|>V_T\end{cases} \tag{21}$$

and

$$\varepsilon''=\begin{cases}\dfrac{\varepsilon_1\tau\omega}{1+\tau^2\omega^2} & \text{for} \quad |V|<V_T \\ \dfrac{\varepsilon_1}{1+\tau\omega} & \text{for} \quad |V|>V_T.\end{cases} \tag{22}$$

Here, $\varepsilon_1(=C_1/C_0)$ is the dielectric constant due to domain walls, and $\varepsilon_2(=C_2/C_0)$ is the dielectric constant in the absence of domain walls. $|V|$ stands for the absolute value of the voltage. At $V_{dc}=0$, the dielectric constant due to domain walls can be defined by

$$\varepsilon_{10}=\frac{C_{10}}{C_0}. \tag{23}$$

At the threshold voltage V_T, τ diverges within the approximation made for C_1, leading to divergent dielectric behavior as $\omega\rightarrow 0$. However, intrinsic damping and a distribution in V_T values would eliminate this divergence in real samples. A distribution in values of V_T is expected since a large sample volume is sampled during the measurements. As shown in Fig. 7, I-V characteristics support this idea by showing a rounding at the threshold voltage.

A Gaussian distribution for the values of V_T is therefore assumed:

$$F(V_T,V_{T0},\sigma)=\frac{1}{\sigma\sqrt{2\pi}}\exp\left[-\frac{(V_T-V_{T0})^2}{2\sigma^2}\right]. \tag{24}$$

With the assumption of a Gaussian distribution for the values of V_T, the capacitance C_1 in Eqs. (19) and (20) needs to be modified as $C_1=C_{av}$, where C_{av} is the average value for C_1 and given by

$$C_{av}=\int_{-\infty}^{\infty}\frac{C_{10}\ \exp[-(V_T-V_{T0})^2/2\sigma^2]}{\sigma\sqrt{2\pi(1-V_{DC}^2/V_T^2)}}dV_T. \tag{25}$$

During integration, the integrand in Eq. (25) is multiplied by i for $|V_T|<V_{dc}$ representing a change from a capacitive response to a resistive response.

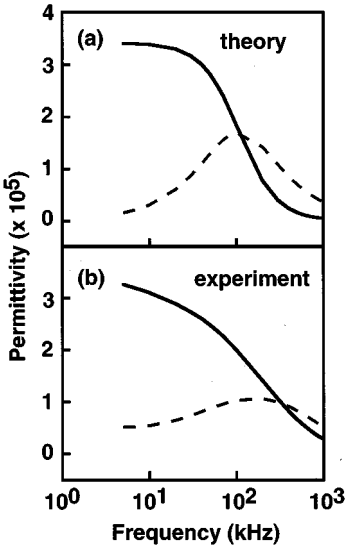

FIG. 13. (a) The calculated real (solid line) and imaginary (dotted line) parts of the dielectric constant for the sample S-2 at $V_{dc}=0$ V as a function of frequency in log scale. (b) The measured real (solid line) and imaginary (dotted line) parts of the dielectric constant for the sample S-2 at $V_{dc}=0$ V as a function of frequency in log scale.

V. COMPARISONS BETWEEN EXPERIMENT AND THEORY

The dielectric constants as a function of ω and V_{dc} were calculated with an assumption of a Gaussian distribution for the values of V_T. These results for S-2 are presented in Figs. 13, 14, 15. Those for S-10 were presented previously.[17]

In Fig. 13(a), the solid line and the dotted line show the calculated ε' and ε'', respectively, as a function of frequency, while the experimental data for the sample S-2 at $V_{dc}=0$ V were shown in Fig. 13(b). For parameter values of $\varepsilon_{10}=110{,}000$, $\varepsilon_2=800$, and $R=12\ \Omega$, the theoretical results were in good agreement with those obtained by experiment. Parameters of 10 and 4.7 V were used for the average threshold V_{T0} and its standard deviation, respectively, for the Gaussian distribution.

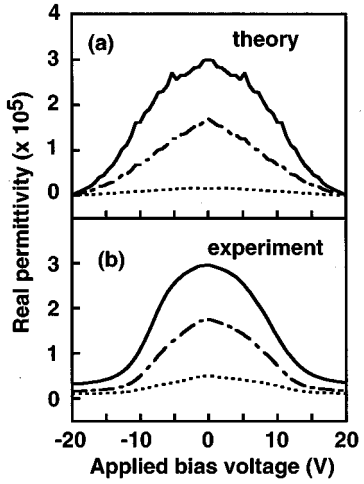

FIG. 14. (a) The calculated ε' for S-2 as a function of applied dc bias at three different ac signal frequencies of 10 kHz (solid line), 100 kHz (dot-dashed line), 500 kHz (dotted line). (b) Measured ε' for S-2 as a function of applied dc bias at three different ac signal frequencies of 10 kHz (solid line), 100 kHz (dot-dashed line), 500 kHz (dotted line).

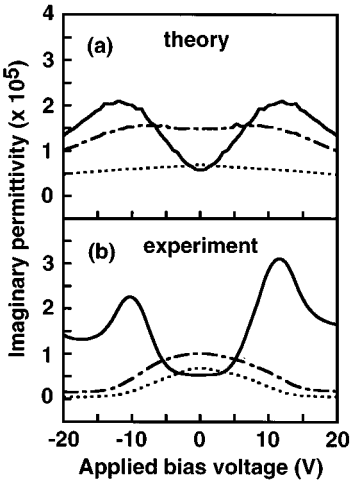

FIG. 15. (a) The calculated ε'' for S-2 as a function of applied dc bias at three different ac signal frequencies of 10 kHz (solid line), 100 kHz (dot-dashed line), 500 kHz (dotted line). (b) The measured ε'' for S-2 as a function of applied dc bias at three different ac signal frequencies of 10 kHz (solid line), 100 kHz (dot-dashed line), 500 kHz (dotted line).

By using Eq. (12) and $C_{10}=C_0\varepsilon_{10}=(L/2)\varepsilon_0\varepsilon_{10}$, the pinning potential period, λ, can be expressed as

$$\lambda=\frac{\pi\varepsilon_0\varepsilon_{10}V_{T0}}{P_s}, \tag{26}$$

where ε_0 is the vacuum permittivity. λ was calculated as 44 ± 21 μm by using a value of $P_s=0.7$ C/m^2 for the polarization determined from the lattice parameter measurements. Within the error bars, this value for λ is equal to the center-to-center electrode spacing. From Eq. (11), the domain-wall pinning energy, e_d was determined as 0.98 ± 0.46 J/m^2, which is very close to the calculated domain-wall pair creation energy of 0.48 J/m^2.[8,9] These are in good agreement with those for S-10.[17] It should be noted that the value of a used in Eq. (3) was estimated by dividing the voltage difference by the center-to-center electrode spacing. It should be viewed as a rough estimate. However, this would not effect the value for λ. A precise value for a can be obtained by properly integrating the field distribution over the volume of the sample. The values determined for λ and e_d suggest that the electrode pattern deposited plays a crucial role in controlling domain-wall dynamics. Below the threshold voltage the domain-wall lattice oscillates between neighboring electrodes. Pinning results from the nucleation barrier to the creation of new domain walls.

Figures 14(a) and 15(a) show the calculated ε' and ε'', respectively, as a function of applied dc bias at three different ac signal frequencies, 10, 100, 500 kHz, using the parameters determined previously. As can be seen, the agreement with the measurements presented for S-2 in Figs. 14(b) and 15(b) is reasonably good, without having any adjustable parameters. Particularly, agreement is very good at low dc bias

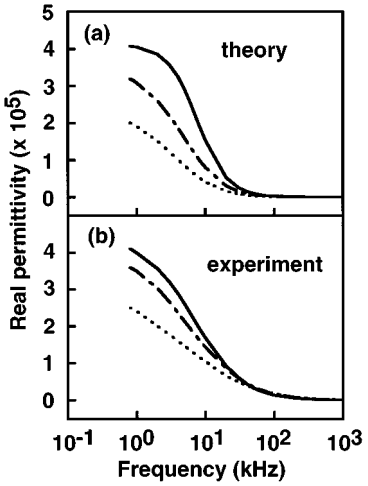

FIG. 16. (a) The calculated ε' for *S*-10 as a function of ac signal frequency at three different dc bias voltages of 0 V (solid line), 3 V (dot-dashed line), 5 V (dotted line). (b) Measured ε' for *S*-10 as a function of ac signal frequency at three different dc bias voltages of 0 V (solid line), 3 V (dot-dashed line), 5 V (dotted line).

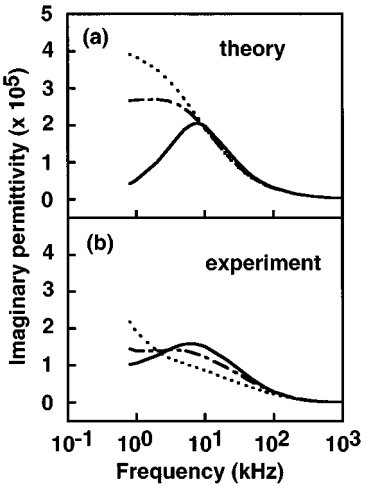

FIG. 17. (a) The calculated ε'' for *S*-10 as a function of ac signal frequency at three different dc bias voltages of 0 V (solid line), 3 V (dot-dashed line), 5 V (dotted line). (b) The measured ε'' for *S*-10 as a function of ac signal frequency at three different dc bias voltages of 0 V (solid line), 3 V (dot-dashed line), 5 V (dotted line).

voltages. However, the deviation becomes significant at dc-bias voltages higher than the threshold voltage. As noted earlier,[17] this may be an indication that the sinusoidal approximation for the pinning potential is only appropriate at low voltages.

The dependence of frequency dispersion on dc bias field for *S*-10 was investigated to elucidate the polarization mechanism better. Figures 16(a) and 17(a) show the calculated ε' and ε'', respectively, as a function of ac signal frequency at three different applied dc bias voltages of 0, 3, and 5 V, using the parameters determined previously. Agreement with measurements for *S*-10 presented in Figs. 16(b) and 17(b) are reasonably good, again without using any adjustable parameters. The larger difference between the calculated and experimental curves shown in Fig. 17 can be attributed to the larger sensitivity of ε'' on field distributions and configurational details which cannot be effectively investigated.

VI. CONCLUSIONS

Heterostructures consisting of epitaxial ferroelectric $PbTiO_3$ and paraelectric $Pb_{1-x}La_xTiO_3$ thin films with $x=0.28$ were grown on (100)-oriented $SrTiO_3$ single-crystal substrates using the metalorganic chemical vapor deposition technique. With a modulation wavelength of about 100 Å, PT/PLT superlattices showed a single diffraction peak in θ–2θ XRD measurements, indicating that the layers are coherent and the superlattice is in a paraelectric phase. At larger modulation wavelengths, several bulklike diffraction peaks were observed, indicating that the PT layers have *a* and *c* domains in a ferroelectric phase.

The dynamical properties of epitaxial ferroelectric heterostructures have been investigated by measuring the dielectric response under external electric fields. A phenomenon with a giant permittivity was observed, and was interpreted by using a model based on the motion of a domain-wall lattice in a sinusoidal potential. The good agreement between the experimental and theoretical results suggests that the deposited interdigitated electrode pattern plays a crucial role in controlling domain-wall dynamics. Below the threshold voltage, pinning comes from a nucleation barrier to the creation of new domain walls, leading to giant permittivity.

These results suggest a cornucopia of new measurements including studies on the effects of temperature, doping, electrode geometry, and modulation wavelength of the superlattice. High dielectric constants up to 400 000 may be obtained at frequencies up to microwaves by increasing the conductivity of the ferroelectric superlattices through impurity doping. Finally, the external control of domain-wall dynamics in these material systems should open up new device applications.

ACKNOWLEDGMENTS

The authors would like to acknowledge A. Zangwill for helpful discussions and a critical reading of the manuscript. This work was supported in part by the NSF Low-Cost Electronic Packaging Research Center, and in part by ARPA.

*Present address: Process Development Team 2, Semiconductor R&D Center, Samsung Electronics Co., Ltd., Yongin-Goon, Kyungki-Do, 449-900, South Korea.

†To whom all correspondence should be addressed.

[1] H. T. Grahn, *Semiconductor superlattices: Growth and Electronic Properties* (World Scientific, Singapore, 1995).

[2] T. Shinjo and T. Takada, *Metallic Superlattices: Artificially Structured Materials* (Elsevier, New York, 1987).

[3] Michael G. Cottam, *Linear and Nonlinear Spin Waves in Magnetic Films and Superlattices* (World Scientific, Singapore, 1994).

[4] Ivan Bozovic, *Superconducting Superlattices and Multilayers* (SPIE, Bellingham, 1994).

[5] D. Schwenk, F. Fishman, and F. Schwabl, J. Phys. Condens. Matter **2**, 5409 (1990).

[6] M. E. Lines and A. M. Glass, *Principles and Applications of*

Ferroelectrics and Related Materials (Clarendon, Oxford, 1977).

[7] Y. Xu, *Ferroelectric Materials and Their Applications* (North-Holland, Amsterdam, 1991).

[8] B. S. Kwak, A. Erbil, B. J. Wilkens, J. D. Budai, M. F. Chisholm, and L. A. Boatner, Phys. Rev. Lett. **68**, 3733 (1992).

[9] B. S. Kwak, A. Erbil, J. D. Budai, M. F. Chisholm, L. A. Boatner, and B. J. Wilkens, Phys. Rev. B **49**, 14 865 (1994).

[10] A. L. Roitburd, Phys. Status Solidi A **37**, 329 (1976); in *Heteroepitaxy of Dissimilar Materials*, edited by R. F. C. Farrow, J. P. Harbison, P. S. Peercy, and A. Zangwill, MRS Symposia Proceedings No. 221 (Material Research Society, Pittsburgh, 1991).

[11] R. Bruinsma and A. Zangwill, J. Phys. (Paris) **47**, 2055 (1986).

[12] B. Horovitz, G. R. Barsh, and J. A. Krumhansl, Phys. Rev. B **43**, 1021 (1991).

[13] J. S. Speck and W. Pompe, J. Appl. Phys. **76**, 466 (1994).

[14] J. S. Speck, A. Seifert, W. Pompe, and R. Ramesh, J. Appl. Phys. **76**, 477 (1994).

[15] G. Gruner, Rev. Mod. Phys. **60**, 1129 (1988).

[16] V. Ambegaokar and B. I. Halperin, Phys. Rev. Lett. **22**, 1364 (1969).

[17] A. Erbil, Y. Kim, and R. A. Gerhardt, Phys. Rev. Lett. **77**, 1628 (1996).

[18] T. Shiosaki, M. Adachi, S. Mochizuki, and A. Kawabata, Ferroelectrics **63**, 227 (1985).

[19] G. W. Farnell, I. A. Cermak, P. Silvester, and S. K. Wong, IEEE Trans. Sonics Ultrason. **SU-17**, 188 (1970).

[20] A. R. Von Hippel, *Dielectric Materials and Applications* (Chapman & Hall, London, 1954), pp. 301.

[21] Y. Kim, Y. H. Han, A. Erbil, and L. A. Boatner, in *Ferroelectric Thin Films IV*, edited by B. A. Tuttle, S. B. Desu, R. Ramesh, and T. Shiosaki, MRS Symposia No. 361 (Material Research Society, Boston, 1994), p. 313.

[22] Y. Kim and A. Erbil (unpublished).

[23] S. G. Joshi and R. M. White, J. Acoust. Soc. Am. **46**, 17 (1969).

[24] A. R. von Hippel, *Dielectrics and Waves* (M. I. T. Press, Crambridge, 1954).